
Article:
Matsubara, M., Stevenson, W., Yabuki, J. et al. (8 more authors) (2017) A Low-Symmetry Cubic Mesophase of Dendronized CdS Nanoparticles and Their Structure-Dependent Photoluminescence. Chem, 2 (6). pp. 860-876. ISSN 2451-9308

https://doi.org/10.1016/j.chempr.2017.05.001

Article Type

A New Low-Symmetry Cubic Mesophase of Dendronized CdS Nanoparticles and their Structure-dependent Photoluminescence Behavior

Masaki Matsubara,[1,5] Warren Stevenson,[2] Jun Yabuki,[1] Xiangbing Zeng,[2] Haoliang Dong,[2] Kazunobu Kojima,[1] Shigefusa F. Chichibu,[1] Kaoru Tamada,[3] Atsushi Muramatsu,[1] Goran Ungar,[2,4,*] and Kiyoshi Kanie[1,*]

[1]Institute of Multidisciplinary Research for Advanced Material, Tohoku University, Katahira 2-1-1, Aoba-ku, Sendai 980-8577, Japan
[2]Department of Materials Science and Engineering, University of Sheffield, Sheffield S1 3JD, U.K.
[3]Institute for Materials Chemistry and Engineering, Kyushu University, 744 Motooka, Nishi-ku, Fukuoka 819-0395, Japan
[4]Department of Physics, Zhejiang Sci-Tech University, Xiasha College Park, 310018 Hangzhou, China
[5]Present address: Department of Materials and Environmental Engineering, National Institute of Technology, Sendai College, 48 Nodayama. Medeshima-Shiote, Natori 981-1239, Japan
*Correspondence: kanie@tagen.tohoku.ac.jp; g.ungar@sheffield.ac.uk

SUMMARY

A new liquid crystal (LC) phase with *P*2$_1$3 symmetry, the lowest so far in a cubic LC, was obtained in a system of CdS quantum dots (QDs) modified with a two-layer corona of aliphatic thiols (inner) and LC aromatic dendrons (outer). We propose that the unusual low symmetry of this cubic mesophase is a result of the multi-layered corona, which prefers to adopt an anisotropic radial profile due to the combination of long and short "bristles". The anisotropic distribution of dendrons (long bristles) in the *P*2$_1$3 phase is thought to facilitate π-π interaction among the aromatic moieties. The interaction gives rise to non-radiative exciton energy transfer pathways which induce photoluminescence quenching of the CdS QDs. This is believed to be the first example of structure-dependent emission-quenching behavior.

Keywords

Dendrimers • GISAXS • Liquid Crystals • Organic-Inorganic Hybrid Materials • Quantum Dots

The Bigger Picture

Quantum dots (QDs) possess size dependent absorption and emission properties which are desirable for creating multi-bandgap photovoltaic devices such as solar cells. It has been theorized that 3-D arrangements of monodisperse QDs, with very small interparticle spacings, may lead to high photon conversion efficiencies due to strong electronic coupling. As such a method of achieving and precisely controlling 3-D inter-particle organization is of paramount importance. In this study a new anisotropic 3-D lattice of monodisperse QDs was formed with interparticle separation distances determined by a two layer ligand coating; the layer thicknesses were in turn dependent on the length and surface density of the ligands. The tailorable self-organization and the 'high absorption, low re-emission' properties of the ordered 3-D phase may prove to be a promising advance towards more efficient solar cells such as dye-sensitized up-conversion emission enhancement.

Highlights

- Double-shell modified CdS quantum dots with liquid crystalline dendrimers
- A new cubic liquid crystal with spacegroup $P2_13$, the lowest cubic symmetry so far
- Unusual quenching of CdS photoluminescence of dendronized CdS in the $P2_13$ phase, presumed to arise from the formation of non-radiative pathways through π-stacking of aromatic dendron ligands

TOC blurb

Self-assembling quantum dots (QDs) have been obtained by attaching an outer corona of aromatic liquid crystalline (LC) dendrons to the surface of an inner alkylthiol corona encapsulating CdS nanoparticles. The dendronized CdS QDs form a cubic LC structure with an unusually low $P2_13$ symmetry. The anisotropic distribution of dendrons in the QD organic corona and in the $P2_13$ LC superlattice is thought to facilitate stacking interactions between the aromatic moieties. Moreover, the dendronized CdS QDs show LC structure-dependent photoluminescence quenching.

INTRODUCTION

Semiconductor nanoparticles (NPs), known as quantum dots (QDs), have attracted a great deal of scientific attention due to their size-dependent and tunable light absorption and emission properties.[1,2] In particular, periodic arrays of QDs have considerable potential in photovoltaics,[3-5] in novel nano-electronic devices where interactions of electronic charge and spin between QDs are expected,[6,7] as well as in efficient thermoelectric devices where high electronic but low phonon conduction is required.[8] As these future devices rely on quantum phenomena such as tunneling of charge and spin, the arrangement of the QDs as well as their separation lengths, typically in the range of nanometers to tens of nanometers, are of prime importance. There have been reports of two-dimensional QD arrays created by epitaxial growth on substrates.[9,10] Surface-modified QDs have been utilized to obtain stable dispersions in anisotropic media of liquid crystals for photonic applications.[11-16] Furthermore, semiconductor NP/dendrimer composites have been obtained by synthesis of QDs in dendrimer templates.[17-19] However, fabrication of 2-D or 3-D arrays of QDs with interparticle distances on the scale of nanometers to tens of nanometers has never been achieved either by bottom-up or top-down methods.

In general, self-organization is a powerful means of forming NP-based periodic structures. For example, a conspicuous variety of binary NP lattices have been obtained by self-organization of two different types of NPs,[20,21] while self-complementary DNA[22-24] and hydrophilic surfactants[25] have been found to promote spontaneous cubic arrangements of NPs. In addition liquid crystalline (LC) phases of ordered NP arrays have been achieved by grafting the particle surfaces with various calamitic,[26-31] bent-core,[32] and dendritic[33] mesogens. These techniques have also the potential to facilitate and precisely control ordered arrangement of QDs.

In our recent study, we described an LC organic-inorganic hybrid dendrimer with a two-layer corona.[34,35] The supramolecular dendrimer, having a spherical gold core, an inner corona of aliphatic thiol ligands and an outer dendron corona, was shown to form an unusual hexagonal superlattice as well as a phase with simple cubic (*SC*) packing of gold

NPs.[34] In the present study, we have advanced this idea to create an organic-inorganic hybrid dendrimer in which a similar two-shell corona now encapsulates a CdS NP (Figure 1). As a result, we report a novel NP superlattice, space-group $P2_13$ which, at the same time, represents a new cubic mesophase of unprecedentedly low symmetry. The specific ordered arrangement of the dendritic ligands within the structure is believed to be responsible for the observed photoluminescence (PL) quenching within the material.

RESULTS AND DISCUSSION

Liquid Crystalline Dendron Molecules. We synthesized a phenethyl ether-type dendron, abbreviated **Dend,** with an amino group at the apex (Figure 1B). Details of the synthesis and characterization of **Dend** are described in our previous paper.[34,35] In pure **Dend** compound the molecules spontaneously assemble into spherical aggregates 9.8 nm in diameter which, above 55 ℃, arrange in a dodecagonal quasicrystal phase that melts at 80°C.[34] In order to induce CdS quantum dots to form ordered arrays, in this work the same dendrons are attached as the outer corona, through amidation, to the carboxylic groups at the surface of the inner aliphatic corona encapsulating the QDs.

Characterization of CdS QDs as Inner Core. The CO_2H-modified CdS QDs, abbreviated **QD-CO_2H** (Figure 2A), were synthesized by the method of Kanehara *et al.*[36] with some modifications using 12-dodecanethiol (DT) and 16-mercapto hexadecanoic acid (MHA) as thiol ligands. In our previous study we have shown that, to obtain a well-ordered self-organized structure, an optimum amount of dendron is required in the outer corona.[34] Control of CO_2H content in **QD-CO_2H** was achieved by optimizing the molar ratio of the DT/MHA mixture in the synthesis of **QD-CO_2H**.

As shown in Figure 2A, the shape of **QD-CO_2H** is close to spherical with narrow size distribution. The mean diameter of the CdS core is 3.9 nm, with the standard deviation of the particle size distribution being 0.4 nm. In order to determine the ratio of DT and MHA on the surface of NPs, the thiols were isolated from the CdS core by I_2-decomposition.[37] Having used a 1:1 DT/MHA molar mixture in the preparation of **QD-CO_2H, the** modification ratio on the surface of the resulting **QD-CO_2H** was 10/3.2 as determined by ^{1}H-NMR. The lowered MHA fraction might have been due to the lower solubility of MHA compared to that of DT in dioctyl ether used in CdS-QDs synthesis. Ratios of attached DT and MHA resulting from the use of other starting reactant mixtures are given in SI, Sect. 2. The resulting **QD-CO_2H** was well dispersed in $CHCl_3$ and CH_2Cl_2 to form a pale yellow transparent stable dispersion. Thermogravimetric (TG) analysis showed that the weight loss of **QD-CO_2H** was 40.4%. This value is attributed to the burning off of DT and MHA. The average numbers of DT (N_{DT}) and MHA (N_{MHA}) molecules per CdS NP were 207 and 66, calculated from the results of ^{1}H-NMR and TG measurements. Detailed calculations are given in the SI.

Modification Number of Dendron in the Outer Corona. Modification of **QD-CO_2H** to obtain dendronized CdS quantum dots, abbreviated **QD-Dend,** was carried out by amidation reaction described in ref. 34. The number of **Dend** molecules per nanoparticle was N_D = 69 – see Section 3.1 in SI; the N_D/N_{MHA} ratio in **QD-Dend** was therefore 1.05. The fact that

the N_D/N_{MHA} ratio was close to 1 meant that the optimized amidation reaction with **Dend** proceeded almost stoichiometrically. This high yield of amidation is partly the result of the choice of alkyl chain lengths in the inner corona, with the longer MHA chains allowing the CO_2H groups to protrude from the surface making them more accessible to the reaction. After **Dend** modification, dispersion-cast NPs tend to form ordered hexagonal monolayers with an interparticle spacing of *ca*. 9 nm (Figure 2B).

Thermal Behavior of QD-Dend. The differential scanning calorimetry (DSC) thermogram of **QD-Dend** is shown in SI, Section 3.3. The second heating trace shows three endotherms, a large one at 7 °C, and two very small ones at 133, and 216 ℃. The material is rigid below the first endotherm and is subject to degradation above the third endotherm. The thermal behavior was similar to our previous system using gold NPs.[34,35] The endotherms at 7 ℃ and 216 ℃, observed here, are attributed to melting of the alkyl chains and isotropization, respectively.

To investigate the 3-D self-organization of **QD-Dend**, transmission small-angle X-ray scattering (SAXS) was recorded on a bulk sample at different temperatures (see Figure S6 in SI). At 50 ℃, **QD-Dend** showed only broad scattering peaks, resulting from the form factor of the nanoparticles in a disordered spatial arrangement. This situation persisted at higher temperatures, although at 150°C some weak sharp diffraction peaks started to emerge. In order to obtain a degree of preferred orientation and resolve the Bragg reflections spatially, thin films of **QD-Dend** were investigated during annealing at 150°C using grazing incidence SAXS (GISAXS). Initially, a strong diffuse peak was observed, indicating the absence of a well ordered structure (Figure 3A). However after 12 hours annealing, three Bragg reflections were detected signifying the development of long-range order (Figure 3B). After 19 hours, additional reflections appeared, indicating further perfection of the ordered structure (Figure 3C,D). Similar annealing behavior has been observed previously with **Dend**-coated gold NPs.[34] The ratio of reciprocal spacings corresponding to the reflections observed in the present **QD-Dend** sample was $\sqrt{2}:\sqrt{3}:\sqrt{4}:\sqrt{5}:\sqrt{8}:\sqrt{9}:\sqrt{11}$, suggesting a cubic unit cell with lattice parameter a = 11.86 ± 0.05 nm (see Table S1 in the SI). Furthermore, the sole systematic absence of Bragg (h00) reflections h = odd rules out all but two possible space groups: $P2_13$ (No. 198) or $P4_232$ (No. 208).[38] The choice between the two space groups was made using the weight-to-volume fraction conversions of the TG results, approximating the density of the CdS and organics as 4.82 g/cm^3 and 0.9 g/cm^3 respectively. According to the calculation, CdS occupies 9.4% of the unit cell (157 nm^3) which, if divided by the volume of a 3.9 nm spherical particle (as determined by TEM), suggests that each contains five CdS NPs; however, a site multiplicity of five is absent in the above space groups. In the case of $P4_232$, special positions with multiplicities of four and six, as well as two (4 + 2 = 6), all introduce additional systematic extinctions that are disobeyed by the GISAXS pattern. For space group $P2_13$, a site multiplicity of four is the only solution that agrees with the observed systematic absences. If the CdS volume is divided amongst only four NPs they must have a slightly larger diameter of 4.2 nm, which is in reasonable agreement with the value of 3.9 nm determined by TEM.

Reconstruction of Electron Density Map. In order to confirm our hypothesis of the structure a simulated diffraction pattern was fitted to the

observed data (Table 1). It was necessary to calculate the phase angles of the structure factors for this non-centrosymmetric space group, hence reconstruct the electron density map. The relative intensity of each Bragg reflection was calculated using structure factor equations for perfect 4.2 nm spheres centred at special positions: (*x, x, x*), (-*x*+½, -*x*, *x*+½), (-*x*, *x*+½, -*x*+½), and (*x*+½, -*x*+½, -*x*). The simulated relative intensities were then matched to the Lorentz-corrected intensity measurements by varying the '*x*' value of the particle positions and $\sqrt{\langle u^2 \rangle}$, their root mean squared (RMS) displacement from the ideal locations.

The reconstruction shows that the unit cell contains four points of high electron density in the configuration described by space group $P2_13$ (*x* = 0.198) – see Figure 4A-C. We attribute the non-spherical shape of these points to the anisotropic Debye-Waller factor (or "temperature factor") associated with a large RMS displacement (1.22 nm). The non-spherical displacement is consistent with the attached organic ligands restricting movement towards the closest neighboring particles. The $\sqrt{\langle u^2 \rangle}$ = 1.22 nm value should be compared with the standard deviation of 0.4 nm in CdS core size distribution determined from TEM to realize how the thick soft corona cushions the effect of core non-uniformity and allows nanoparticles to form LC arrays with 3-D long-range order in spite of their polydispersity.

The $P2_13$ arrangement of the dendronized quantum dots is closely related to the face centred cubic (*FCC*) structure; the two structures are in fact identical in the special case when *x* = 0. An *FCC* LC structure has recently been reported for gold NPs coated with side-on attached rod-like mesogens,[30] however it has been noted that neither of the "close packed" structures, i.e. *FCC* or hexagonal close packing (*HCP*), have been observed in dendrimers.[39] This has been attributed[40,41] to the supramolecular spheres being soft rather than hard balls, enabling them to pack more efficiently in structures known as Frank-Kasper (FK) phases.[42,43] FK phases contain only the smallest, i.e. tetrahedral,[44] interstices in contrast to *FCC* and *HCP* which both possess large octahedral vacancies whose centres are hard to reach by the ends of the dendron tails. While it is unsurprising that **QD-Dend** did not form a *FCC* structure, it is unusual for mesophases to adopt such low-symmetry and "inefficient" packing modes as $P2_13$. Our previous study on gold NPs coated with the same two-layer corona of DT+MHA (inner) and dendron **Dend** (outer) also had unexpected outcomes: a simple cubic structure was obtained which contains interstices even larger than those of *FCC* and *HCP*.[34] Body centered cubic (*BCC*) structures have also been reported in dendrimers,[39] as well as in dendronized gold NPs,[31] however this structure is similar to a FK phase. Our current two-layered corona design is a promising principle likely to lead to further unprecedented and unusual 3-D LC structures.

Radial Density Profile of Dendronized CdS QDs. In order to relate the properties of the organic corona to the packing mode of the spheres, or "spherical brushes", *dV/dr* functions were calculated and compared in Figure 5 for four packing modes: *FCC*, $Pm\bar{3}n$ or A15 (typical in dendrimers), $P2_13$, and *SC*. The *dV/dr* function[34,45] describes the average volume increase of the spheres as their radius *r* increases from 0. Initially all *dV/dr* functions follow a parabola as $dV/dr \propto r^2$, but once the spheres clash the gradient of each function drops and becomes negative; *dV/dr* reaches zero when all space is filled. The length of the decay after the first point of collision therefore describes the degree of anisotropy that must be

adopted by the brushes in order to fill the remaining space. As illustrated in Figure 5, the packing modes differ by the decay of their *dV/dr* curves. For dendrimers with tails of equal length, packing modes with *dVdr* rapidly decaying to zero are preferred. $Pm\bar{3}n$ is therefore more favorable than *FCC* as the large octahedral vacancies of the latter lengthen the decay of its *dV/dr* function. By contrast, it appears that particles possessing our two-layered corona prefer modes with slowly decaying *dV/dr*, featuring large interparticle voids. We propose that a multi-layered corona prefers to adopt an anisotropic radial profile due to the combination of long and short bristles. In our $P2_13$ structure (x = 0.198), the twelve nearest neighbors of a reference particle are separated into two shells of six, with respective centre-to-centre distances ($2r_0$) of 0.646a and 0.791a. For *FCC* and $P2_13$, the values of r_0 can be read directly from the gradient drops in Figure 5. Converting r_0 to nanometers, we find that the spheres within the $P2_13$ structure expand without obstruction up to r = 3.83 nm. The CdS cores and the alkylthiol ligands combined occupy 43.5% of the unit cell volume (757 nm^3), which if divided amongst four spheres, suggests that **QD-CO$_2$H** reaches a radius of 3.51 nm. The closeness of this approximation to r_0 infers that the minimum interparticle separation within the sample is in this case governed by the thickness of the dense inner corona. Furthermore, the lack of space between nearest neighbor NPs suggests that the dendrons, hence the MHA ligands, are indeed distributed anisotropically around the CdS surface, aggregating in regions that allow them to fill the open interparticle channels (see Figure 6). The proposed reorganization of MHA–**Dend** ligands on the NP surface during annealing is in line with a similar idea proposed previously for gold NPs.[30,31,46] We will return to the distribution of the dendrons below to explain the PL behavior.

Photoluminescence and UV/vis Absorption of Self-Organized QD-Dend. To investigate the PL behavior of **QD-Dend**, a **QD-Dend** film was prepared on hydrophobic quartz glass by casting from a $CHCl_3$ dispersion followed by drying. Figures 7A and B show photographs of the **QD-Dend** film without and with UV irradiation at 365 nm. The film shows strong fluorescence when excited by UV irradiation. It is noteworthy that brightness of the PL is drastically reduced and almost completely quenched, in spite of UV excitation, after annealing the film at 150 ℃ for 20 h (Figure 7C). There is no difference in the size and shape of CdS core before and after annealing, shown in Figure S13 in SI. Under these conditions **QD-Dend** forms the $P2_13$ superlattice.

To clarify such unusual quenching behavior, UV/vis absorption and PL spectra of the **QD-Dend** film were investigated as a function of annealing temperature (T_a). The sample was annealed for 1 h at each T_a, followed by rapid cooling to room temperature under a N_2 positive pressure in the dark. Thereafter the absorption and emission spectra were recorded in air at room temperature. This procedure eliminated the possibility of thermal fluorescence quenching, which is regarded as electron trapping in temporary trapping sites generated at elevated temperatures. An initial T_a of 50 ℃ was chosen and was increased to 150 ℃ in 20 ℃ increments. The LC structures formed during annealing were preserved on cooling due to the high viscosity of the system. The resulting PL and absorption spectra are shown in Figures 7D and E, respectively. The absorption spectra are normalized at 442 nm. The UV/vis absorption and PL spectra of the $P2_13$ structure obtained after the long annealing at 150 ℃ are also shown. As seen in Figure 7D, **QD-Dend** shows two band-edge emissions, consisting of at least two close energy levels at λ = 450 and 470 nm, and

broad defect-trapped (λ ≃ 600 nm) emissions after annealing at 50 ℃. In the case of a **QD-CO_2H** film on quartz glass substrate, only a band-edge emission at λ = 450 nm and broad defect-trapped (λ ≃ 600 nm) emissions were observed (see, Figure S10 in SI). Such emission behavior for **QD-CO_2H** is common for CdS QDs.[47] The result suggests that the band-edge emission of **QD-Dend** at λ = 450 nm is due to the emission from the CdS-QD cores. On the other hand, the band-edge emission at λ = 470 nm, only observed in the bulk film of **QD-Dend**, could be attributed to the formation of a new lower energy state, namely, a dendron-mediated extended state (DMES), by the interaction between CdS-QDs and **Dend** in film form. In a $CHCl_3$ dispersion, the band-edge emission at λ = 470 nm was not observed either before or after annealing of the **QD-Dend** film (See: Figure S11 in SI). This behavior also supports our conclusion that the emission at λ = 470 nm is due to the formation of DMES in the film form on the substrate. We will return to DMES below to clarify the quenching mechanism. A significant decrease in the emission intensity of the peak at 450 nm is observed after annealing at 70 ℃; the peaks at 470 and 600 nm are also quenched but to a lesser extent. Further increases in the annealing temperature led to further decreases in the emission peaks. The reduced PL intensity originating from the defect-trapped sites arises due to quenching of band-edge emissions.[48,49] After annealing at 150 ℃ for 20 h, the band-edge emission at 450 nm was almost completely quenched – Figures 7C, D. Here, **QD-Dend** forms the $P2_13$ LC structure. In contrast to the decreased emission, upon annealing from 50 to 150 ℃ the absorbance of the **QD-Dend** film gradually increased at wavelengths between 450 and 800 nm as well as at < 350 nm (Figure 7E and the inset). Furthermore, the absorbance drastically increased on annealing at 150 ℃ for 20 h. Such large increases in the two wavelength ranges are due to the formation of non-radiative relaxation pathways for emission quenching in the film as described below.

Next, in order to investigate the mechanism of the observed quenching, we measured the emission lifetimes of the **QD-Dend** film by time-resolved PL spectroscopy using a femto-second pulse laser (Figures 8A and B). The excitation wavelength was tuned to 384 nm. To determine the lifetimes of the band-edge emissions at 450 and 470 nm, the time-resolved PL decay of the **QD-Dend** film was collected (before and after annealing) and integrated from 445 to 455 nm and 465 to 475 nm, respectively. The decay curves could be well fitted to a double exponential model described by Equation S8 in the SI. The fitting parameters are summarized in Tables S2 and S3. According to these analyses,[50,51] the initial lifetimes of the fast dominant component of the emissions were 43 ps for the 450 nm peak and 65 ps for the 470 nm peak. The lifetimes were virtually unchanged upon 20 h annealing at 150℃ and were calculated as 41 and 63 ps, respectively. To date, PL emission and quenching phenomena have been explained by a variety of mechanisms, such as energy transfer (ET),[52,53] thermal quenching,[54] electron tunneling,[55] and charge transfer (CT).[56] Especially, emission lifetimes of several tens of pico-seconds of CdS QDs are recognized as recombination towards non-radiative centers (NRC) by non-radiative relaxation through ET.[51] Thus, the lifetimes observed in the present system suggest that ET is the predominant emission-quenching mechanism.

Based on the UV/vis absorption and PL behavior described, we propose, as most plausible, an emission-quenching mechanism based on ET and operative both before and after annealing, as shown in Figures 9A and B,

respectively. Here, band gap energies (E_V's) of PL at 450 nm (emission from the CdS QD cores) and 470 nm (emission from DMES) before annealing the **QD-Dend** were calculated as 2.76 eV and 2.64 eV, respectively, using the following equation $E_V = 1240/\lambda$ (eV). The associated band structure before annealing showing two band-edge emissions is schematically illustrated in Figure 9A. Before annealing, the excitons recombine with the holes and emit at 2.76 eV and 2.64 eV. Here, E_V of **Dend** could be calculated as ~ 4 eV from the absorption spectra of **Dend** (Figure S12). The insulating high E_V restricts the excitons inside the CdS core for the emission. The lifetime for the emission is dominated by recombination towards NRC through ET. After annealing at 150 ℃ for 20 h, the aromatic moieties of **Dend** self-assemble into π-stacked structures (see, Figures 6A and 7E) to form new non-radiative pathways with lower E_V's than that of DMES. Here the E_V's corresponding to DMES and the π-stacking states could be assigned as 2.64 eV and 2.61 eV, respectively, from the absorption edges before and after annealing (see, SI, Section 5.2).[57] Based on this, the PL quenching mechanism after annealing could be as shown schematically in Figure 9B. Here, the excitons (E_V's = 2.76 and 2.64 eV) transfer instantly into the non-radiative π-stacked pathways of narrow band gaps with lower energy levels (E_V = 2.61 eV), rather than recombine with holes at the band edges, which results in PL quenching. In addition to the difference in E_V's before and after annealing, derived from the absorption spectra, UV absorbance of **QD-Dend** is found to gradually increase at successive annealing temperatures at wavelengths between 450 and 800 nm (Figure 7E). The E_V at 800 nm corresponds to E_V = 1.6 eV. This narrow band gap might also contribute to the non-radiative PL quenching. Figure S12 shows UV/vis spectra of **QD-Dend** annealed at 50 ℃ for 1 h and 150 ℃ for 20 h in $CHCl_3$ dispersion. No increase in absorbance is seen in the 450-800 nm range in dispersion. This result adds support to the proposition that the annealing-induced increase in UV/vis absorption in **QD-Dend** film is due to the π-stacked structure. We also calculated the QD size from the wavelength of the absorption peak in $CHCl_3$ dispersion using an equation[58]. As the result, the particle mean diameters both of before and after annealing could be assigned as 4.0 nm. The result was in good agreement with the particle mean diameters determined by the TEM observations (Figure 2 and Figure S13).

Next we consider possible mechanisms of formation of the π-stacked structure that is clearly associated with the development of the $P2_13$ self-assembly. We propose that the anisotropic distribution of the two ligand types, required to fill the inter-particle space, enables the formation of long-range aromatic networks as depicted schematically (blue color) in Figure 6A. As the $P2_13$ superlattice gradually forms, the dendrons begin to cluster in the interparticle voids, leading to increased aromatic π-stacking in the local environment of the QDs. The modified electronic state of the π-stacked aromatic moieties is thought to provide a non-radiative pathway for QD carrier de-excitation via ET. The probability of PL emission is then progressively reduced by the increasing concentration of π-stacked moieties in the vicinity of the QDs. This is the most plausible explanation of the unusual quenching behavior observed in the present case. Amrutha *et al.* have reported decreased PL intensity due to π-stacking in oligophenylenevinylene films.[59] In their study, an increase in absorption intensity around 250 nm and > 500 nm was observed. A comparison of this and other reports[60,61] with our present findings strongly supports our hypothesis that the development of a π-stacked aromatic network, associated with formation of the $P2_13$ structure, plays a key role in the PL

behavior of **QD-Dend**. To our knowledge, this is the first example of PL quenching of QDs induced by a change in supramolecular assembly.

To obtain additional confirmation that PL quenching is indeed related to the mode of self-assembly, the 20 h annealed **QD-Dend** film was re-dispersed in $CHCl_3$ and re-cast on a quartz substrate to obtain again an amorphous **QD-Dend** film. The re-cast film showed strong PL, similar to that observed before annealing of the original film (shown in Figure 10). The UV/vis absorption behavior also reverted to that before annealing. The amorphous (re-cast) **QD-Dend** film with recovered emission was then re-annealed at 150 ℃, which res ulted again in quenching of its PL emission. Such reversibility of emission/quenching can be seen after the 3rd redispersion-casting-annealing cycle (shown in SI, Figure S8). The time-resolved PL measurements revealed that the lifetimes of the band-edge emissions at 450 nm and 470 nm for the re-cast **QD-Dend** film were 32 ps and 41 ps, respectively (see, Figure 8). These lifetimes became slightly shorter than those of the original unannealed and annealed **QD-Dend** film, indicating some decrease in ET efficiency. In general these results give further support to our conclusion that the quenching is due to the formation of the π-stacked self-organized structure and, indirectly, also to the notion of thiol ligand reorganization on particle surface.

CONCLUSION

In conclusion, we have synthesized CdS quantum dots surrounded by a double shell dendron-based soft corona that assemble in a new low-symmetry cubic LC phase. The annealing-induced transition from disorder to cubic order is accompanied by strong quenching of photoluminescence. This is attributed to the creation of non-radiative energy transfer pathways via π-stacking of aromatic dendrons in the cubic phase. Such behavior points the way to designing materials with tunable fluorescence quenching, Regarding the mesophase structure, this work is the first report of a $P2_13$ cubic LC phase, and is believed to be the first record of a superlattice of NPs of such low symmetry. The principle, applied here, of embedding NPs in a double-shell soft corona promises to lead to further novel structured arrays of QDs and other nanoparticles, particularly for plasmonic materials. In addition, our radial density profile *dV/dr* based model is shown to provide a rational, semi-quantitative relationship between the density profile across the soft corona, and the resulting superlattice. This observed PL behavior offers the possibility of developing QD-based energy-conversion materials for e.g. up-conversion emission enhanced photovoltaic cells through addition of dyes excited at long wavelengths,[62,63] thermally conducting materials[8] and light emitting diodes. The present thermal phase transition-induced PL quenching could be utilized in thermal devices such as thermal history monitors on heat-sensitive products.

EXPERIMENTAL PROCDURES

Synthesis of CdS QDs. CO_2H-modified CdS QDs **QD-CO_2H** were synthesized in the presence of 12-dodecanethiol (DT) and 16-mercapto hexadecanoic acid (MHA) as thiol ligands. The synthetic procedure for the preparation of the CO_2H-modified CdS quantum dots is as follows: Initially, cadmium stearate (204 mg, 0.30 mmol), 1,1,3,3-tetramethyl-2-thiourea (20 mg, 0.15 mmol), DT (15.2 mg, 0.075 mmol), and MHA (21.6 mg, 0.075

mmol) were dissolved into 10 mL of dioctyl ether. Then, the solution was heated at 150 ℃ for 2 h, and subsequently at 230 ℃ for 3 h under an N_2 atmosphere. The resulting solution was centrifuged and washed with $CHCl_3$/EtOH three times to remove excess amount of thiols. The residue was dried under reduced pressure, so that CO_2H-modified CdS quantum dots **QD-CO_2H** were synthesized.

Dendron Modification of CdS Quantum Dots. Modification of **QD-CO_2H** to obtain dendronized CdS QDs **QD-Dend** was carried out by amidation reaction. A representative procedure was as follows: A mixed solution of **QD-CO_2H** (50 mg) and **Dend** (250 mg) in CH_2Cl_2 (10 mL) was added to 200 mg of *N*,*N*'-dicyclohexylcarbodimide at room temperature under an argon atmosphere. The resulting mixture was stirred at the room temperature for 12 h. The reaction mixture was then centrifuged and washed twenty times with $CHCl_3$/MeOH to remove the non-reacted **Dend**. Complete removal of free **Dend** from **QD-Dend** was ascertained by ^{1}H-NMR and GPC measurements of the supernatant solutions. The precipitate was dried under reduced pressure to give dendron-modified **QD-Dend** as a yellow colored viscous solid. The formation of amide bonding was observed by infrared spectroscopy (see Section 3.2 in SI).

GISAXS Measurement. Thin film samples of **QD-Dend** were prepared by casting from $CHCl_3$ dispersion on silicon substrates. GISAXS experiments were carried out at station I16, Diamond Light Source. The sample was mounted on a 6-circle goniometer for control of the angle and position of the incident beam on the sample. A Dectris Pilatus-2M area detector was used for collection of GISAXS patterns. A flight tube flushed with flowing helium was inserted between the sample and the detector, in order to cut down the background noise due to air scattering from the main beam. An adjustable tapered beam-stop was positioned inside the flight tube near the detector end. The annealing of the sample was carried out using a programmable vacuum oven. The GISAXS patterns used in this study were recorded at room temperature, but it was ascertained, using high-temperature GISAXS, that the patterns before and after cooling from the annealing temperature did not change.

Emission and Absorption Measurement of the Dendronized CdS. PL spectra were recorded using a Hitachi F-2700 fluorescence spectrophotometer. UV/vis spectra were collected at room temperature in the reflection mode using a Hitachi U-3900 spectrophotometer equipped with an integrating sphere. The **QD-Dend** film was prepared on a hydrophobic quartz glass by casting from $CHCl_3$ dispersion. The sample was annealed for 1 h at each T_a under a N_2 positive pressure in the dark, followed by rapid cooling to room temperature. T_a was increased from 50 to 150 ℃ in 20 ℃ increments. Therefore both PL and absorption spectra were recorded at room temperature after annealing. This procedure eliminated the possibility of thermal quenching at high temperatures. As comparisons, the temperature variable UV/vis and PL behavior of a **Dend** film on a hydrophobic quartz glass in Figure S14.

Time-resolved PL Measurement. The samples were prepared following the same procedure used to observe the emission and absorption behaviors. The time-resolved PL measurements were carried out using a frequency-doubled Al_2O_3:Ti laser (384 nm, 125 nJ/cm^2 a pulse) and a streak camera as the excitation source and detector, respectively.

SUPPLEMENTAL INFORMATION

Supplemental Information includes 14 figures and three tables.

AUTHOR CONTRIBUTIONS

Study design: M.M., K.Ka., A.M. Conducting studies: M.M., W.S., J.Y., X.Z., H.D., K.Ka., G.U. Structure Analysis: W.S., X.Z., H.D., G.U. Photoluminescence Analysis: M.M., J.Y., K.Ko., S.F.C., K.T., K.Ka. Manuscript preparation: M.M., K.Ka., W.S., G.U. Manuscript editing: All authors.

ACKNOWLEDGMENTS

For help with X-ray synchrotron experiments we thank Dr. G. Nisbet and Prof. S. Collins of beamline I16 and Prof. N. Terrill of I22 at Diamond Light Source. We also acknowledge Dr. M. Nakaya and Mr. I. Tanaka for the synthesis of CdS NPs. The authors thank JSPS (Research fellowship for young scientists No. 24•9313 (MM), Grant-in-aid for young scientific research (A) No. 22685019 (KKa), Grant-in-aid for scientific research (B) No. 25288087 and 16H04190 (KKa), and Bilateral Joint Research Projects (KKa)), the Asahi Glass Foundation (KKa), METI & NEDO Super Hybrid Materials Development Project (AM, KKa), MEXT the Management Expenses Grants for National Universities Corporations (KKo, SFC, KT, AM, KKa), the NSF-EPSRC Pire program, project “RENEW” (EP-K034308), the Leverhulme Foundation (RPG-2012-804), and the 1000 Talents Program of P.R. China (GU) for funding this work.

REFERENCES AND NOTES

1. Kim, J. Y., Voznyy, O., Zhitomirsky, D., Sargent, E. H. (2013). 25th Anniversary Article: Colloidal Quantum Dot Materials and Devices: A Quarter-Century of Advances. Adv. Mater. *25*, 4986-5010.
2. Trindade, T., O’Brien, P., Pickett, N. L. (2001). Nanocrystalline semiconductors: synthesis, properties, and perspectives. Chem. Mater. *13*, 3843-3858.
3. Brongersma, M. L., Cui, Y., Fan, S. (2014). Light management for photovoltaics using high-index nanostructures. Nat. Mater. *13*, 451-460.
4. Kongkanand, A., Tvrdy, K., Takechi, K., Kuno, M., Kamat, P. V. (2008). Quantum dot solar cells. Tuning photoresponse through size and shape control of CdSe−TiO_2 architecture. J. Am. Chem. Soc. *130*, 4007-4015.
5. Ren, S., Chang, L.-Y., Lim, S.-K., Smith, M., Zhao, N., Bulović, V., Bawendi, M., Gradecak, S. (2011). Inorganic–organic hybrid solar cell: Bridging quantum dots to conjugated polymer nanowires. Nano Lett. *11*, 3998-4002.
6. Hines, D. A., Kamat, P. V. (2014). Recent advances in quantum dot surface chemistry. ACS Appl. Mater. Interfaces *6*, 3041-3057.
7. Chekhovich, E. A., Makhonin, M. N., Tartakovskii, A. I., Yacoby, A., Bluhm, H., Nowack, K. C., Vandersypen, L. M. K. (2013). Nuclear spin effects in semiconductor quantum dots. Nat. Mater. *12*, 494-504.
8. Urban, J. J. (2015). Prospects for thermoelectricity in quantum dot hybrid arrays. Nat. Nanotechnol. *10*, 997–1001.
9. Hull, R., Floro, J., Graham, J., Gray, J., Gherasimova, M., Portavoce, A., Ross, F. M. (2008). Synthesis and functionalization of epitaxial quantum dot nanostructures for nanoelectronic architectures. Mater. Sci. Semicond. Process. *11*, 160-168.

10. Springholz, G., Holy, V., Pinczolits, M., Bauer, G. (1998). Self-organized growth of three-dimensional quantum-dot crystals with fcc-like stacking and a tunable lattice constant. Science *282*, 734-737.
11. Mirzaei, J., Reznikov, M., Hegmann, T. (2012). Quantum dots as liquid crystal dopants. J. Mater. Chem. *22*, 22350-22365.
12. Rodarte, A. L., Nuno, Z. S., Cao, B. H., Pandolfi, R. J., Quint, M. T., Ghosh, S., Hein, J. E., Hirst, L. S. (2014). Tuning Quantum-Dot Organization in Liquid Crystals for Robust Photonic Applications. ChemPhysChem *15*, 1413-1421.
13. Rodarte, A. L., Pandolfi, R. J., Ghosh, S., Hirst, L. S. (2013). Quantum dot/liquid crystal composite materials: self-assembly driven by liquid crystal phase transition templating. J. Mater. Chem. C *1*, 5527-5532.
14. Rodarte, A. L., Shcherbatyuk, G. V., Shcherbatyuk, L., Hirst, L. S., Ghosh, S. (2012). Dynamics of spontaneous emission of quantum dots in a one-dimensional cholesteric liquid crystal photonic cavity. RSC Adv. *2*, 12759-12763.
15. Prodanov, M. F., Pogorelova, N. V., Kryshtal, A. P., Klymchenko, A. S., Mely, Y., Semynozhenko, V. P., Krivoshey, A. I., Reznikov, Y. A., Yarmolenko, S. N., Goodby, J. W., Vashchenko, V. V. (2013). Thermodynamically stable dispersions of quantum dots in a nematic liquid crystal. Langmuir *29*, 9301-9309
16. Kumar, M., Kumar, S. (2015). Luminescent CdTe quantum dots incarcerated in a columnar matrix of discotic liquid crystals for optoelectronic applications. RSC Adv. *5*, 1262-1267.
17. Yamamoto, D., Koshiyama, T., Watanabe, S., Miyahara, M. T. (2015). Synthesis and photoluminescence characterization of dendrimer-encapsulated CdS quantum dots. Colloids and Surfaces A: Physicochem. Eng. Aspects *411*, 12-17.
18. Lemon, B. I., Crooks, R. M. (2000). Preparation and characterization of dendrimer-encapsulated CdS semiconductor quantum dots. J. Am. Chem. Soc. *122*, 12886-12887.
19. Lakowicz, J. R., Gryczynski, I., Gryczynski, Z., Murphy, C. J. (1999). Luminescence spectral properties of CdS nanoparticles. J. Phys. Chem. B *103*, 7613-7620.
20. Shevchenko, E. V., Talapin, D. V., Kotov, N. A., O'Brien, S., Murray, C. B. (2006). Structural diversity in binary nanoparticle superlattices. Nature *439*, 55-59.
21. Chen, Z., Moore, J., Radtke, G., Sirringhaus, H., O'Brien, S. (2007). Binary nanoparticle superlattices in the semiconductor−semiconductor system: CdTe and CdSe. J. Am. Chem. Soc. *129*, 15702-15709.
22. Zhang, C., Macfarlane, R. J., Young, K. L., Choi, C. H. J., Hao, L., Auyeung, E., Liu, G., Zhou, X., Mirkin, C. A. (2013). A general approach to DNA-programmable atom equivalents. Nat. Mater. *12*, 741-746.
23. Park, S. Y., Lytton-Jean, A. K. R., Lee, B., Weigand, S., Schatz, G. C., Mirkin, C. A. (2008). DNA-programmable nanoparticle crystallization. Nature *451*, 553-556.
24. Nykypanchuk, D., Maye, M. M., van der Lelie, D., Gang, O. (2008). DNA-guided crystallization of colloidal nanoparticles. Nature *451*, 549-552.
25. Fan, H., Leve, E., Gabaldon, J., Wright, A., Haddad, R. E., Brinker, C. J. (2005). Ordered two- and three-dimensional arrays self-assembled from water-soluble nanocrystal–micelles. Adv. Mater. *17*, 2587-2590.
26. Kanie, K., Sugimoto, T. (2003). Organic−inorganic hybrid liquid crystals: Hybridization of calamitic liquid-crystalline amines with

monodispersed anisotropic TiO_2 nanoparticles. J. Am. Chem. Soc. *125*, 10518-10519.
27. Kanie, K., Muramatsu, A. (2005). Organic−inorganic hybrid liquid crystals: Thermotropic mesophases formed by hybridization of liquid-crystalline phosphates and monodispersed α-Fe_2O_3 particles. J. Am. Chem. Soc. *127*, 11578-11579.
28. Lewandowski, W., Fruhnert, M., Mieczkowski, J., Rockstuhl, C., Górecka, E. (2015). Dynamically self-assembled silver nanoparticles as a thermally tunable metamaterial. Nat. Commun. *6*, 6590. | DOI: 10.1038/ncomms7590.
29. Zeng, X. B., Liu, F., Fowler, A. G., Ungar, G., Cseh, L., Mehl, G. H., Macdonald, J. E. (2009). 3D ordered gold strings by coating nanoparticles with mesogens. Adv. Mater. *21*, 1746-1750.
30. Mang, X., Zeng, X. B., Tang, B., Liu, F., Ungar, G., Zhang, R., Cseh, L., Mehl, G. H. (2012). Control of anisotropic self-assembly of gold nanoparticles coated with mesogens. J. Mater. Chem. *22*, 11101-11106.
31. Wojcik, M., Kolpaczynska, M., Pociecha, D., Mieczkowski, J., Gorecka, E. (2010). Multidimensional structures made by gold nanoparticles with shape-adaptive grafting layers. Soft Matter *6*, 5397-5400.
32. Marx, V. M., Girgis, H., Heiney, P. A., Hegmann, T. (2008). Bent-core liquid crystal (LC) decorated gold nanoclusters: synthesis, self-assembly, and effects in mixtures with bent-core LC hosts. J. Mater. Chem. *18*, 2983-2994.
33. Donnio, B., García-Vázquez, P., Gallani, J. L., Guillon, D., Terazzi, E. (2007). Dendronized ferromagnetic gold nanoparticles self-organized in a thermotropic cubic phase. Adv. Mater. *19*, 3534-3539.
34. Kanie, K., Matsubara, M., Zeng, X. B., Liu, F., Ungar, G., Nakamura, H., Muramatsu, A. (2012). Simple cubic packing of gold nanoparticles through rational design of their dendrimeric corona. J. Am. Chem. Soc. *134*, 808-811.
35. Matsubara, M., Miyazaki, A., Zeng, X. Muramatsu, A., Ungar, G., Kanie, K. (2015). Rheology of thermotropic liquid-crystalline dendron-modified gold nanoparticles. Mol. Cryst. Liq. Cryst. *617*, 50-57.
36. Kanehara, M., Arakawa, H., Honda, T., Saruyama, M., Teranishi, T. (2012). Large-scale synthesis of high-quality metal sulfide semiconductor quantum dots with tunable surface-plasmon resonance frequencies. Chem. Eur. J. *18*, 9230.
37. Templeton, A. C., Hostetler, M. J., Warmoth, E. K., Chen, S., Hartshorn, C. M., Krishnamurthy, V. M., Forbes, M. D. E., Murray, R. W. (1998). Gateway reactions to diverse, polyfunctional monolayer-protected gold clusters. J. Am. Chem. Soc. *120*, 4845-4849.
38. Hahn, T. (1996). International Tables of Crystallography Vol. A: Spacegroup Symmetry 4th ed. (Netherlands: Kluwer Academic).
39. Ungar, G., Liu, F., Zeng, X. B. (2014). Thermotropic Cubic Liquid Crystal Phases, Other 3D Phases and Quasicrystals, Chap. 7 in Handbook of Liquid Crystals, 2nd ed., Vol. 5, Goodby, J. W., Collings, P. J., Kato, T., Tschierske, C., Gleeson, H. F., Raynes, P., eds., (Weinheim, Germany: Wiley-VCH Verlag GmbH) pp. 363-436.
40. Ungar, G., Zeng, X. B. (2005). Frank–Kasper, quasicrystalline and related phases in liquid crystals. Soft Matter *1*, 95-106.
41. Li, Y. Y., Lin, S. T., Goddard III, W. A. (2004). Efficiency of various lattices from hard ball to soft ball: Theoretical study of thermodynamic properties of dendrimer liquid crystal from atomistic simulation. J. Am. Chem. Soc. *126*, 1872-1885.

42. Frank, F. C., Kasper, J. S. (1959). Complex alloy structures regarded as sphere packings. II. Analysis and classification of representative structures. Acta Crystallogr. *12*, 483.
43. Hajiw, S., Pansu, B., Sadoc, J. F. (2015). Evidence for a C14 Frank–Kasper phase in one-size gold nanoparticle superlattices. ACS Nano *8*, 8116-8121.
44. Sinha, A. K. (1972). Topologically Closed Packed Structures in Transition Metal Alloys. (Oxford: Pergamon Press).
45. Ungar, G., Liu, Y., Zeng, X. B., Percec, V., Cho, W.-D. (2003). Giant supramolecular liquid crystal lattice. Science *299*, 1208-1211.
46. Liu, X., Yu, M., Kim, H., Mameli, M., Stellacci, F. (2012). Determination of monolayer-protected gold nanoparticle ligand–shell morphology using NMR. Nat. Commun. *3*, 1182.
47. Ouyang, J., Kuijper, J., Brot, S., Kingston, D., Wu, X., Leek, D. M., Hu, M. Z., Ripmeester, J. A., Yu, K. (2009). Photoluminescent colloidal CdS nanocrystals with high quality via noninjection one-pot synthesis in 1-octadecene. J. Phys. Chem. C. *113*, 7579-7593.
48. O'Neil, M., Marohn, J., McLendon, G. (1990). Picosecond measurements of exciton trapping in semiconductor clusters. Chem. Phys. Lett. *168*, 208-210.
49. Veamatahau, A., Jiang, B., Seifert, T., Makuta, S., Latham, K., Kanehara, M., Teranishi, T., Tachibana, Y. (2015). Origin of surface trap states in CdS quantum dots: relationship between size dependent photoluminescence and sulfur vacancy trap states. Phys. Chem. Chem. Phys. *17*, 2850-2858.
50. Zhang, J. Z., O'Neil, R. H., Roberti, T. W. (1994). Femtosecond studies of interfacial electron-hole recombination in aqueous CdS colloids. Appl. Phys. Lett. *64*, 1989-1991.
51. Wheeler, D. A. Zhang, J. Z. (2013). Exciton Dynamics in Semiconductor Nanocrystals. Adv. Mater. *25*, 2878-2896.
52. Medintz, I., Hildebrandt, N. (2013). FRET - Förster Resonance Energy Transfer From Theory to Applications. (Weinheim, Germany:Wiley-VCH Verlag GmbH).
53. Sapsford, K. E., Berti, L., Medintz, I. L. (2006). Materials for fluorescence resonance energy transfer analysis: beyond traditional donor-acceptor combinations. Angew. Chem. Int. Ed. *45*, 4562–4588.
54. Valerini, D., Cretí, A., Lomascolo, M. (2005). Temperature dependence of the photoluminescence properties of colloidal CdSe⁄ZnS core/shell quantum dots embedded in a polystyrene matrix. Phys. Rev. B *71*, 235409.
55. Zen'kevich, É. I., Blaudeck, Th., Heidernätsch, M., Cichos, F., von Borczyskowski, C. (2009). Effects of electron tunneling and nonresonance quenching of photoluminescence in semiconducting CdSe/ZnS AND CdSe nanocrystals by porphyrin molecules in joint complexes. Theor. Exp. Chem. *45*, 23-34.
56. Algar, W. R., Stewart, M. H., Scott, A. M., Moon, W. J., Medintz, I. L. (2014). Quantum dots as platforms for charge transfer-based biosensing: challenges and opportunities. J. Mater. Chem. B *2*, 7816.
57. Mariappan, R., Ragavendar, M., Ponnuswamy, V. (2011). Growth and characterization of chemical bath deposited $Cd_{1-x}Zn_xS$ thin films. J. Alloys Compd. *509*, 7337-7343.
58. Yu, W. W., Qu, L., Guo, W., Peng, X. (2003). Experimental Determination of the Extinction Coefficient of CdTe, CdSe, and CdS Nanocrystals. Chem. Mater. *15*, 2854-2860.
59. Amrutha, S. R., Jayakannan, M. (2008). Probing the π-stacking induced molecular aggregation in π-conjugated polymers, oligomers,

and their blends of p-phenylenevinylene. J. Phys. Chem. B *112*, 1119-1129.
60. Valeur, B., Berberan-Santos, M. N. (2012). Molecular Fluorescence: Principles and Applications, 2nd ed. (Weinheim, Germany: Wiley-VCH Verlag GmbH).
61. Hong, Y., Lama, J. W. Y., Tang, B. Z. (2009). Aggregation-induced emission: phenomenon, mechanism and applications. Chem. Commun. 4332-4353.
62. Nozik, A. J., Beard, M. C., Luther, J. M., Law, M., Ellingson, R. J., Johnson, J. C. (2010). Semiconductor quantum dots and quantum dot arrays and applications of multiple exciton generation to third-generation photovoltaic solar cells. Chem. Rev. *110*, 6873–6890.
63. Bae, S.-H., Zhao, H., Hsieh, Y.-T., Zuo, L., De Marco, N., Rim, Y. S., Li, G., Yang, Y. (2016). Printable solar cells from advanced solution-processible materials. Chem *1*, 197-219.

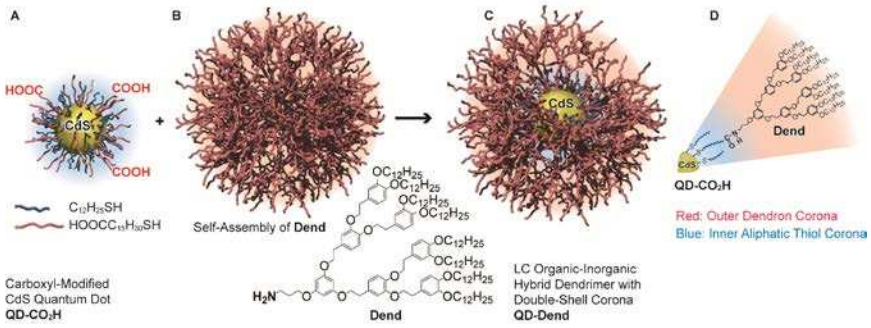

Figure 1. Schematic depictions of dendronized CdS QDs.
CdS QDs were modified with a two-layer corona of mixed alky thiols and carboxyalkyl thiol (inner) and aromatic-aliphatic LC dendrons (outer).
(A) A carboxyl-modified CdS QD, **QD-CO_2H**, with an inner aliphatic thiol corona.
(B) Chemical structure of **Dend** in the outer corona (bottom) and a self-assembled nanosphere of pure **Dend** (top).
(C) The organic-inorganic hybrid LC dendrimer, **QD-Dend**, with a double-shell corona.
(D) Chemical structure of the double corona.

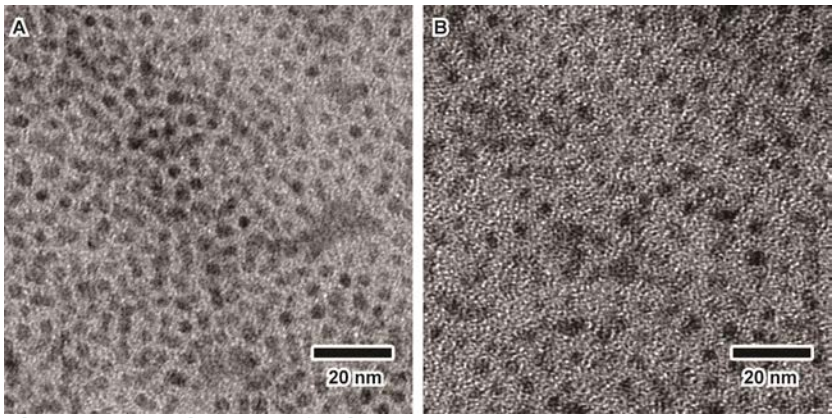

Figure 2. TEM images of CdS QDs

The mean size of the CdS core of **QD-CO_2H** is 3.9 ± 0.4 nm, and the shape of **QD-CO_2H** is close to spherical.

(A) CO_2H-modified CdS QDs **QD-CO_2H**.

(B) Dendronized CdS QDs **QD-Dend**.

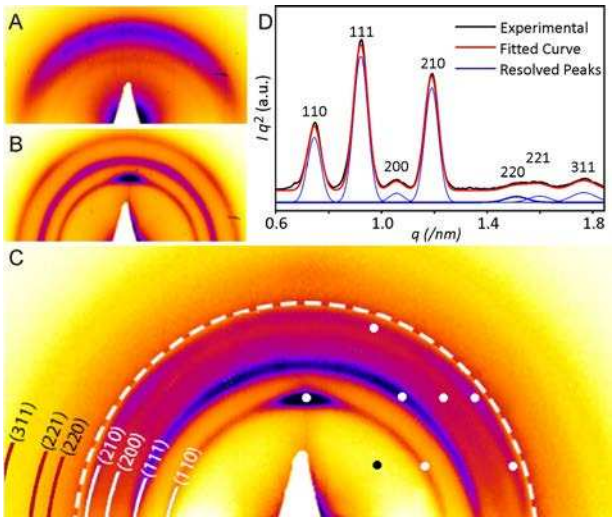

Figure 3. GISAXS patterns of QD-Dend

GISAXS patterns of **QD-Dend** after (A) 6 hours, (B) 12 hours and (C) 19 hours of annealing at 150 °C. Three Bragg reflections are observed after 12 hours of annealing (B). and another four weak ones after 19 hours (C). The region outside the dashed line in (C) was recorded with a longer exposure. The white spots are the expected positions of the Bragg maxima of the observed reflections assuming a cubic structure with [110] vertical. The black spot shows the expected position of the missing (100) peak, indicating the reflection condition *h*00 = 2n. (D) 1-D azimuthally averaged and Lorentz-corrected diffractogram based on (C), showing numerically resolved peaks; the experimental (background-subtracted) and the fitted curves are superimposed, and are vertically displaced for clarity.

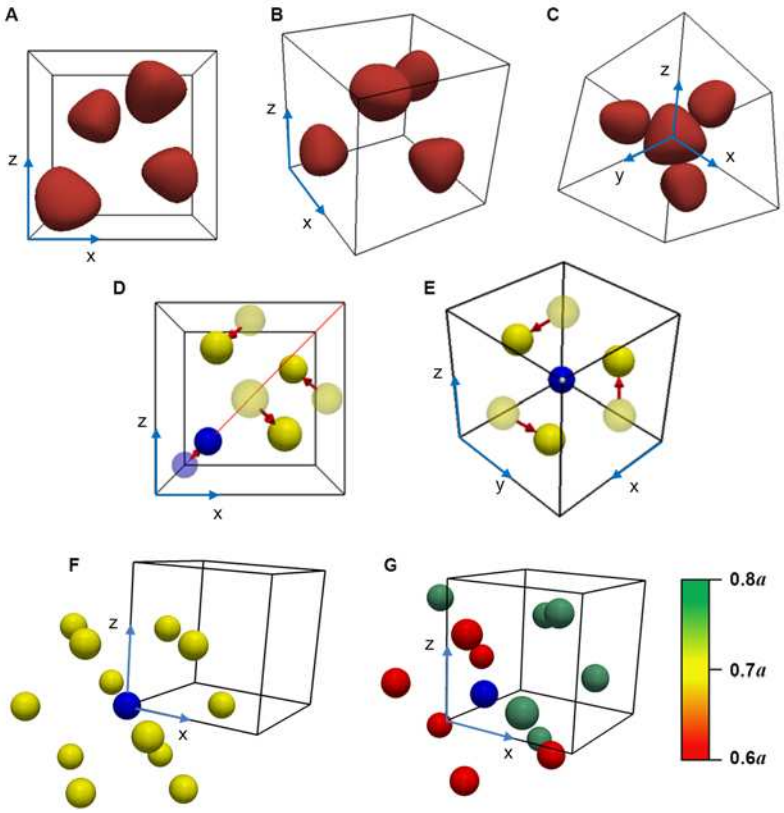

Figure 4. Electron density maps.
(A)-(C) The single isosurface presentation of the electron density map reconstructed using the integrated intensities and phase angles shown in Table 1; views along [100] (A), an arbitrary axis (B), and [111] (C). The surfaces each enclose a high-density volume equal to that of a 4.2 nm sphere. (D,E) The unit cell transformation from *FCC* (hollow spheres) to $P2_13$ (solid spheres); views along the [100] and [111], respectively. The displacement is by *x* along one of the [111] directions. Particles which lie outside the cell after the displacement are not shown. (F,G) The 12 nearest neighbors of a reference particle within a *FCC* and a $P2_13$ lattice, respectively. The particles are colored here according to their closeness to the reference particle and are divided amongst three planes perpendicular to the [111] axis. (Particles have been reduced in size for clarity).

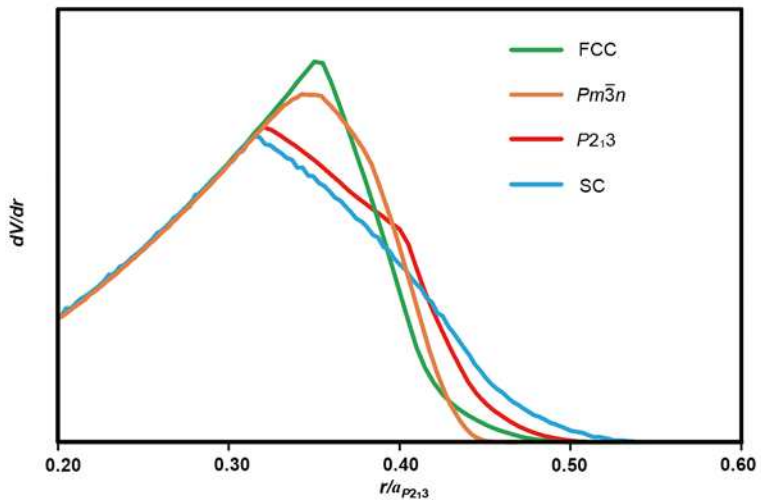

Figure 5. Radial density profiles of dendronized CdS QDs.
Calculated volume increase of an average spherical particle upon radial growth from its center for four cubic packings: *P*2$_1$3, *FCC*, *SC* and $Pm\bar{3}n$ (also known as A15). The *dV/dr* functions were scaled so that final volume enclosed by each of the expanding spheres is equal to the total volume of a single particle. The curves of *SC* and $Pm\bar{3}n$ were then normalized according to the ratio 1:$\sqrt[3]{4}$:$\sqrt[3]{8}$, as the number of spheres in a *SC*, *P*2$_1$3, *FCC* and $Pm\bar{3}n$ unit cell is 1, 4, 4 and 8, respectively. The radius is given as a fraction of the *P*2$_1$3 unit cell parameter.

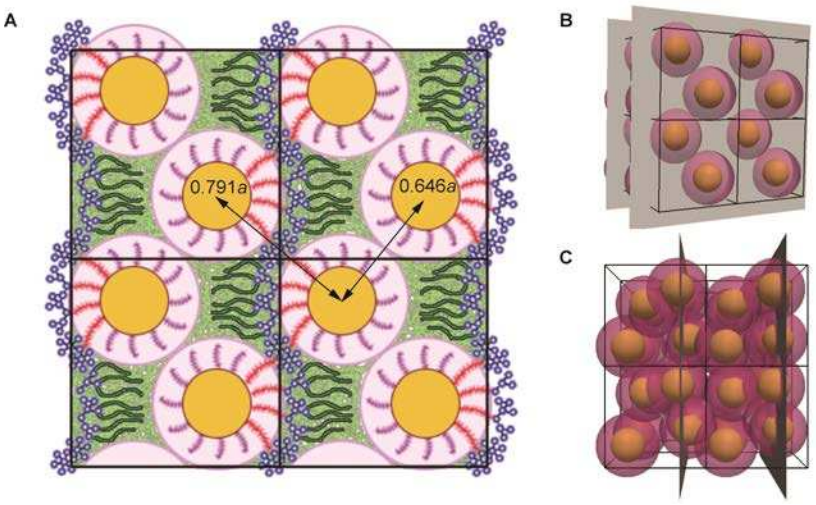

Figure 6. Schematic illustrations of dendronized CdS in $P2_13$ phase. (A) A single plane slice at x = 0.75 parallel to (100) illustrating schematically the general principles of the proposed molecular arrangement within our $P2_13$ structure. Yellow = CdS, pink = DT, red = MHA, blue = aromatic and green = dendron tails. (B,C) Perspective views of the 3-D quantum dot array showing the (100) Miller planes depicted in (A).

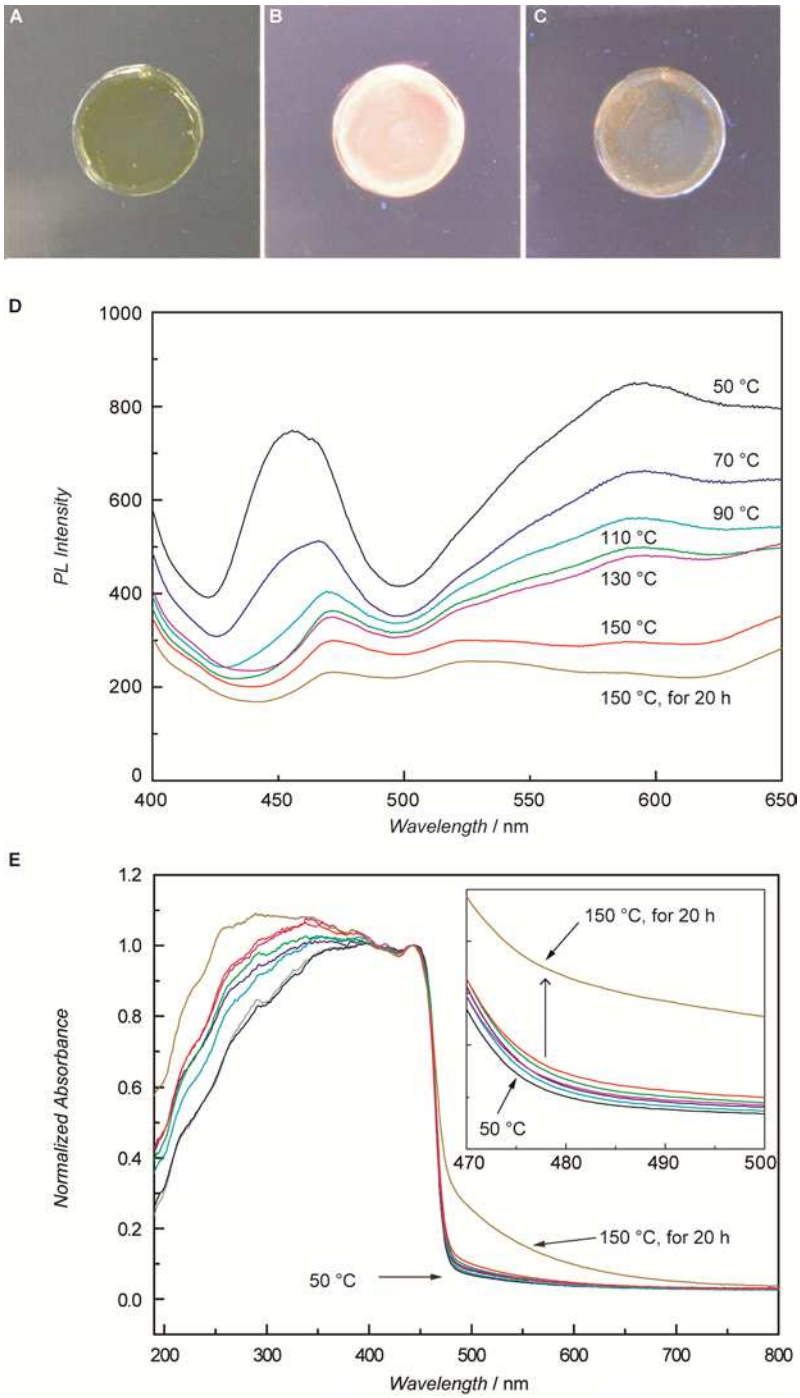

Figure 7. Photoluminescence behavior of dendronized CdS QDs. Photographs of **QD-Dend** on a hydrophobic, circular cover glass. **QD-Dend** was cast from $CHCl_3$ dispersion and dried under Ar atmosphere. (A) As prepared, without UV irradiation. (B) As prepared, under UV irradiation (λ_{ex} = 365 nm). (C) Annealed at 150 ℃ for 20 h, then photographed under UV irradiation (λ_{ex} = 365 nm). PL of **QD-Dend** was almost completely quenched after annealing. (D) Annealing-temperature dependence of PL profiles of **QD-Dend**. PL measurements were carried out after cooling to room temperature. (E) Normalized UV/vis absorption spectra of annealed **QD-Dend**. Inset: magnified between 470 to 500 nm. The line color legend

in (D) also applies to (E). The UV/vis spectra are normalized at 442 nm because the absorption is derived from the CdS cores. Unnormalized absorption spectra are also given in Figure S9 in SI.

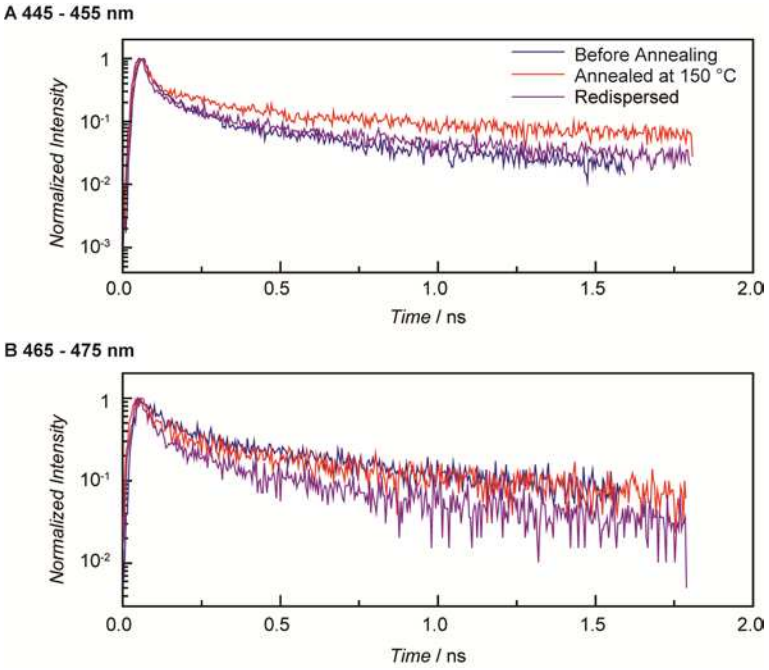

Figure 8. Time resolved PL decays of CdS QDs.
Normalized time resolved PL decays of untreated, annealed, and re-dispersed **QD-Dend** films in two spectral ranges: (A) 445-455 nm and (B) 465-475 nm. The decay curves can be well fitted to a double exponential model (See Section 5.1 in SI). The lifetimes of the fast dominant component of the emission at 450 nm (470 nm) are 43 (65) ps before annealing, 41 (63) ps after annealing, and 32 (41) ps for redispersed **QD-Dend.** The line color legend in (A) also applies to (B). After redispersion the lifetimes became slightly faster than those of the original unannealed and annealed **QD-Dend** film, indicating decreased ET efficiency.

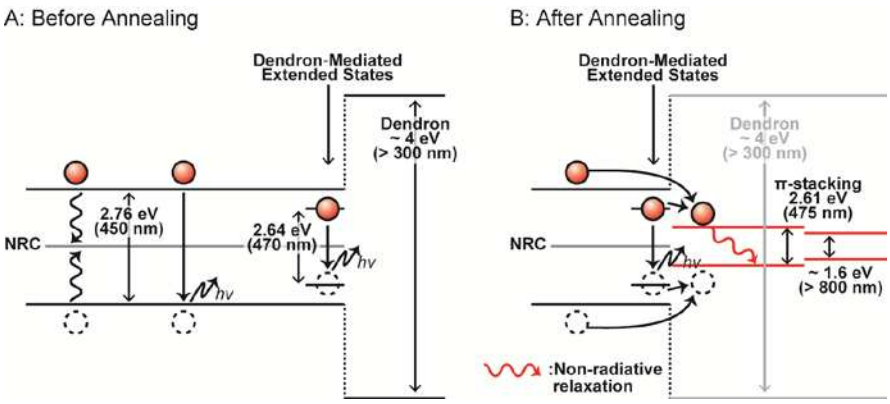

Figure 9. A Schematic Illustration of Emission-Quenching Mechanism.

The most plausible ET model and band structures of **QD-Dend**. (A) Before annealing. The band gap energy of original CdS core is 2.76 eV. The interaction between CdS surface and **Dend** form the lower energy band (dendron-mediated extended states (DMESs)) with the band gap energy of 2.64 eV. Such two band edge structures are responsible for the two band edge emissions of **QD-Dend**. The band gap energy of **Dend** (~ 4 eV) is too high to accept the excitons. (B) After annealing. The aromatic moieties of **Dend** form a non-radiative quenching pathway through π-stacking. The band gap energy was assigned as 2.61 eV from the UV/vis absorption spectra of after annealed **QD-Dend** at 150 ℃ for 20 h. The excitons transfer into the non-radiative pathway, resulting in PL quenching. At DMES, the excitons slightly recombine with holes and show little emission at 470 nm even though the after annealing.

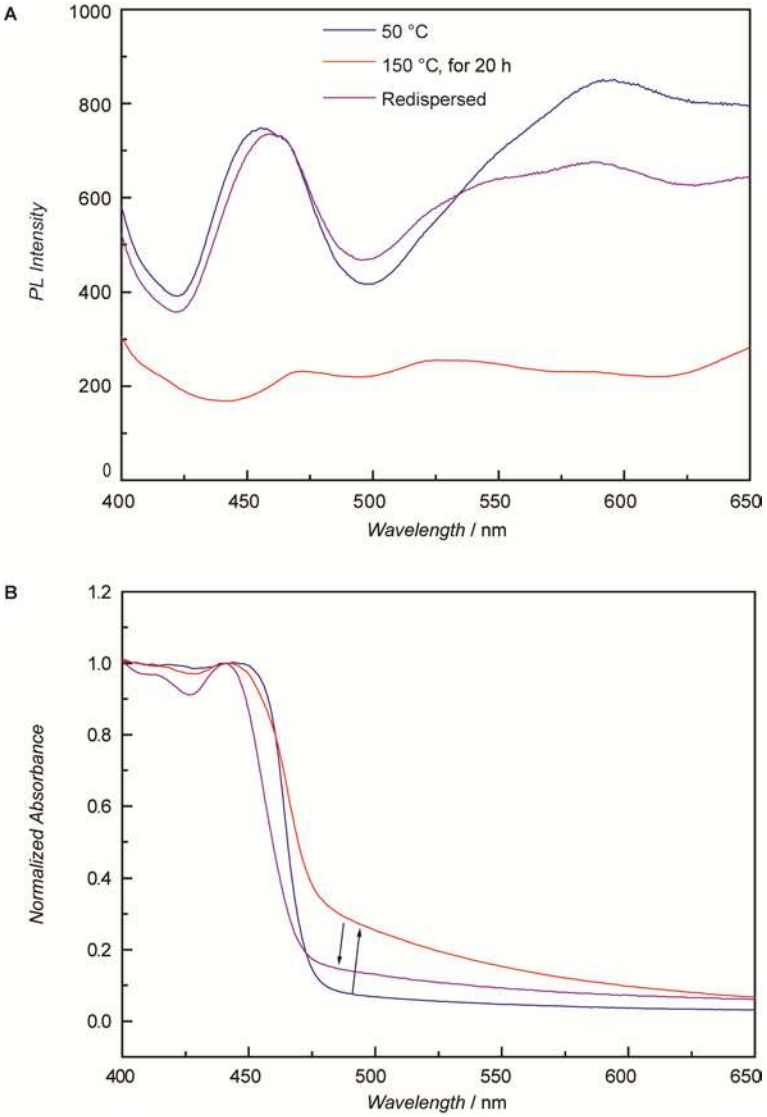

Figure 10. Reversibility on PL and the corresponding absorbance spectra.

(A) PL and (B) Normalized absorbance spectra of annealed and re-dispersed **QD-Dend**. After re-dispersing into $CHCl_3$ and re-casting on glass substrate, the quenched PL intensity was recovered and increased absorption spectra also decreased.

Table 1. The Integrated and Calculated Intensities and Calculated Phase Angles of the Diffraction Peaks.

.

Table 1. The Integrated and Calculated Intensities and Calculated Phase Angles of the Diffraction Peaks.

(*hkl*)	q (nm^{-1})	Multiplicity	Integrated intensity $I_{(hkl)}/I_{(111)}$	Calculated Intensity $I_{(hkl)}/I_{(111)}$	Phase Angle (Rad)
(110)	0.750	12	0.288	0.290	π/2
(111)	0.917	8	1.000	1.000	-1.515
(200)	1.061	6	0.078	0.424	π
(210)	1.174	24	0.607	0.609	π

The best fit was achieved for x = 0.198 and $\sqrt{\langle u^2 \rangle}$ =1.22 nm.

Graphical Abstract.